Research Square

Preprints are preliminary reports that have not undergone peer review.
They should not be considered conclusive, used to inform clinical practice,
or referenced by the media as validated information.

Cation-intercalated copper azide breaks the safety–energy trade-off in primary explosives

Wei-Xiong Zhang

zhangwx6@mail.sysu.edu.cn

Sun Yat-sen University https://orcid.org/0000-0003-0797-3465

Yun-Fan Yan

Sun Yat-sen University

Ming-Yu Guo

Sun Yat-sen University

Qian-You Wang

Beijing Institute of Technology

Meng Cui

Fujian Institute of Research on the Structure of Matter, Chinese Academy of Sciences

Xu-Yang wang

Beijing Institute of Technology

Liu Liu

Sun Yat-sen University

Shuai-Qi Ning

Sun Yat-sen University

Si-Yuan Hao

Sun Yat-sen University

Yu Shang

Sun Yat-sen University

Zi-Luo Fang

Sun Yat-sen University

Xiao-Ming Chen

Sun Yat-sen University https://orcid.org/0000-0002-3353-7918

Physical Sciences - Article

Keywords:

Posted Date: October 6th, 2026

DOI: https://doi.org/10.21203/rs.3.rs-11150011/v1

License: This work is licensed under a Creative Commons Attribution 4.0 International License.
Read Full License

Additional Declarations: Yes there is potential Competing Interest. Sun Yat-sen University has filed a Chinese patent application (No. 202511845814.X) related to this work.

Cation-intercalated copper azide breaks the safety–energy trade-off in primary explosives

Yun-Fan Yan,[1] Ming-Yu Guo,[1] Qian-You Wang,[2] Meng Cui,[3] Xu-Yang Wang,[2] Liu Liu,[1] Shuai-Qi Ning,[1] Si-Yuan Hao,[1] Yu Shang,[1] Zi-Luo Fang,[1] Wei-Xiong Zhang,[1,*] and Xiao-Ming Chen[1]

[1] MOE Key Laboratory of Bioinorganic and Synthetic Chemistry, School of Chemistry, IGCME, Sun Yat-sen University, Guangzhou 510275, (P. R. China)

[2] State Key Laboratory of Explosion Science and Technology and Safety Protection, Beijing Institute of Technology, Beijing 100081, (P. R. China)

[3] State Key Laboratory of Structural Chemistry, Fujian Institute of Research on the Structure of Matter, Chinese Academy of Sciences, Fuzhou 350002, (P. R. China)

*Correspondence: zhangwx6@mail.sysu.edu.cn

Abstract:

Primary explosives convert small external stimuli into intense chemical energy release over nanosecond-to-microsecond timescales, serving as the initial energy source for chemical-to-kinetic systems[1,2]. For over a century, developing practical high-performance alternatives to toxic and underperforming lead azide (**LA**) has remained a critical challenge. To date, no candidate alternatives have been able to simultaneously satisfy the comprehensive criteria of stability, safety, initiation efficiency, environmental compatibility, and cost-effectiveness[3-4]. Here, we establish cation intercalation as a molecular-scale design strategy to break the inherent

safety–energy trade-off of copper azide (CA), which combines excellent detonation performance with extreme handling hazard. This paradigm affords cation-intercalated copper azide (**ICA**), comprising alternating organic cation buffer layers and energetic copper–azide layers. The representative compound $(Et_4N)_2[Cu_8(N_3)_{18}]$ (**ICA-1**, Et_4N^+ = tetraethylammonium) is easily synthesized in high yield from low-cost precursors and comprehensively outperforms **LA**. Its electrostatic safety threshold is 15-fold that of **LA** and 270-fold that of **CA**, with sealed-chamber peak pressure and initiation efficiency reaching 3.3-fold and 10-fold that of **LA**, respectively, enabling chip-scale initiation. Theoretical analyses indicate that intercalants impede phonon propagation to dissipate external stimuli. This work broadens layered materials research and provides a design paradigm for next-generation primary explosives[5-8].

Main

Energetic materials are indispensable thermochemical energy storage systems for aerospace, defence, and civilian industries, where primary explosives serve as the critical initial energy trigger to ensure stable deflagration-to-detonation transition (DDT) and reliable system operation[9-12]. For over a century, lead azide (**LA**) has dominated commercial primary explosive applications, yet its intrinsic lead toxicity and limited initiation efficiency severely restrict modern deployment[13,14]. **LA** requires mixing with an additional ignition agent to compensate for its low flame sensitivity (**Supplementary Fig. 1**)[15,16]. This leads to oversized, inefficient structures unsuitable for miniaturized chip-scale energetic devices. Addressing this issue by developing high-performance, less-toxic **LA** alternatives adaptable to chip-scale energetic devices remains a core research bottleneck in material science[17,18].

Two mainstream strategies have been developed to pursue lead-free alternatives. The first focuses on the design and synthesis of new energetic compounds. Pioneering studies from Klapötke's and Shreeve's groups have yielded a series of energetic nitrogen-rich compounds[19-23] and metal complexes[24], alongside energetic perovskites first reported by our group[25-27], that avoid lead contamination and deliver robust detonation performance owing to efficient heat and gas evolution (**Supplementary Fig. 2**). Nonetheless, these candidates suffer from poor cost-effectiveness, hazardous synthetic routes, and challenges in simultaneously achieving favourable safety and DDT performance. The second strategy aims at the performance optimization of existing non-lead energetic systems. For example, copper azide (**CA**), with 56.9% nitrogen (nearly twice that of **LA**) and excellent properties, is extremely sensitive: slight mechanical stimulus may cause accidental detonation, hindering its practical application. Existing composite modification[15,28,29] and ligand regulation[30-33] provide modest desensitization, restricting industrial application (**Supplementary Fig. 3**).

Layered structural engineering enables intrinsic desensitization *via* interlayer slippage-induced stimulus dissipation and hot-spot suppression, as validated in various layered crystalline systems[34-37]. Nevertheless, limited **CA**-based layered structures relying on direct energetic monolayer stacking fail to simultaneously balance stability, safety (*i.e.*, insensitivity to non-explosive stimuli, where higher thresholds indicate enhanced safety), initiation efficiency, environmental compatibility, and cost-effectiveness[30]. To break this bottleneck, we propose a cation-intercalated copper azide (**ICA**) layers paradigm (**Fig. 1a and Supplementary Fig. 4**). Bulky tetraethylammonium (Et_4N^+) cations intercalate copper–azide ($[Cu_8(N_3)_{18}]^{2-}$) layers, resolving the safety–energy trade-off in primary explosives. The resulting **ICA-1** not

only comprehensively outperforms **LA** in core metrics but also affords notable economic and scalable advantages. This work pioneers an intercalation engineering strategy for energetic crystal modulation, offering a potentially transferable strategy that may enable the design of advanced safe, high-energy thermochemical energy storage systems.

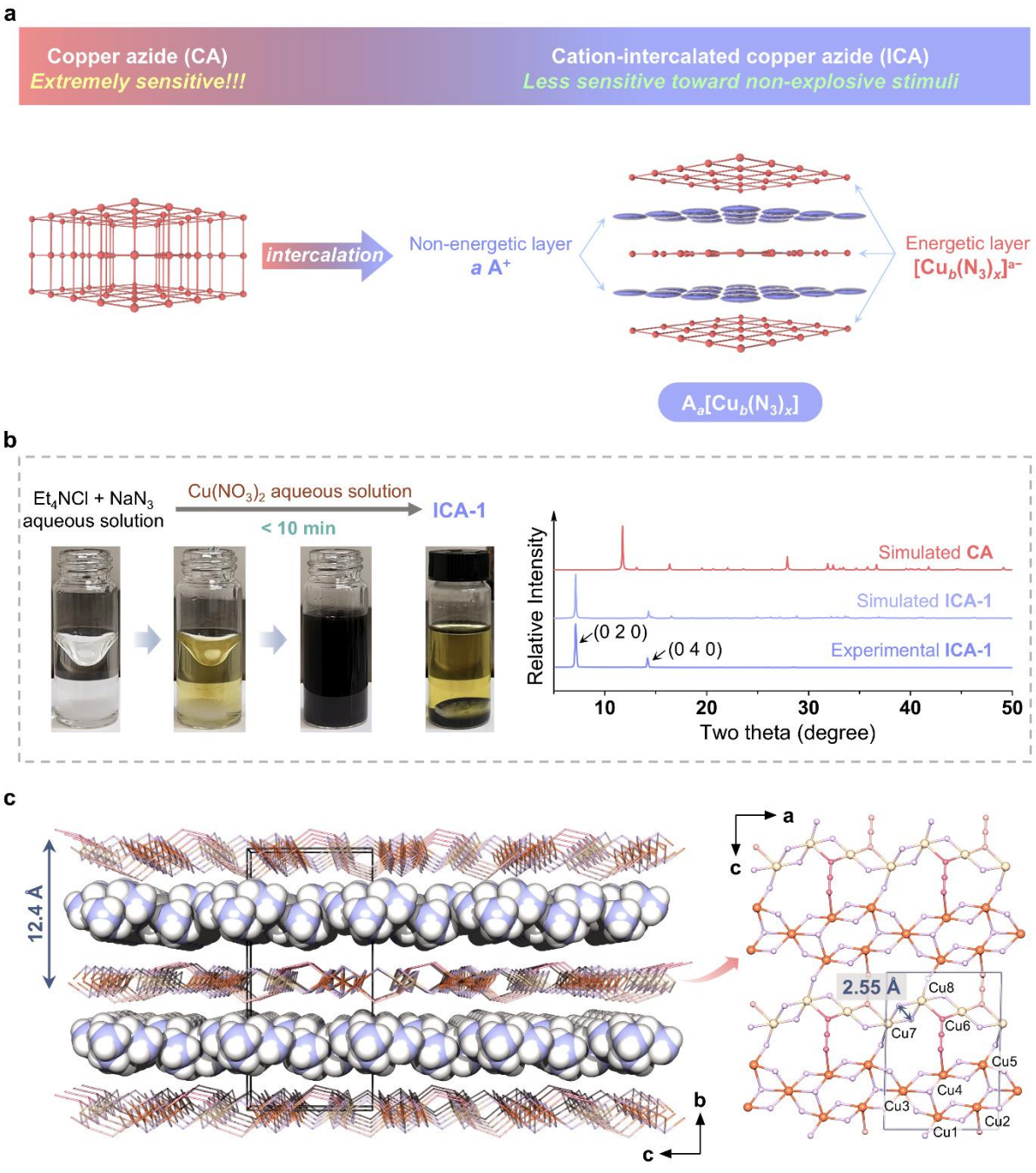

Fig. 1|The design synthesis and structural characterization of ICA-1. a, A new design paradigm for intercalation of **CA** layers with disc-shaped spacer cations into deeply passive and

energetic $(Et_4N)_2[Cu_8(N_3)_{18}]$ (**ICA-1**). **b**, Experimental procedure for the direct synthesis of **ICA-1** and its phase purity. **c**, Crystal structure of **ICA-1**. Copper atoms and nitrogen atoms are coloured differently according to their distinct coordination modes; details are provided in **Supplementary Fig. 11.** For the N_3^- anions acting in the μ-1,1 (end-on) bridge mode, only the coordinated nitrogen atoms are shown, while the rest of the atoms are omitted for clarity.

Synthesis and structural analysis

Upon mixing aqueous copper(II) nitrate solution with an aqueous mixture of tetraethylammonium chloride and sodium azide, the reaction proceeds instantaneously, generating macroscopic black **ICA-1** crystals within minutes (direct synthesis, **Fig. 1b**). The resulting crystals were isolated *via* suction filtration, rinsed with ethanol, and air-dried, affording a high yield of 79% (**Supplementary Fig. 5**). This mild, facile aqueous synthetic strategy utilizes low-cost, commercially available precursors and enables rapid gram-scale synthesis under ambient conditions, implying the industrial scalability of **ICA-1**. Combining high operational safety with minimal time and costs, this protocol represents a superior alternative to previously reported **CA**-based derivatives (**Supplementary Table 1**). Powder X-ray diffraction (PXRD) measurements confirm the high phase purity of **ICA-1** without hazardous **CA**-derived impurities, as the experimental diffraction pattern closely matches the simulated profile while differing substantially from that of pure **CA** (**Fig. 1b**). Notably, **ICA-1** can also be prepared *via* an indirect synthesis route, where **CA** suspension was preformed as an intermediate prior to mixing with the Et_4N^+ cations and supplementary N_3^- anions (**Supplementary Fig. 7**). These results confirm that **ICA-1** exhibits higher thermodynamic

stability and lower solubility than **CA**. This structural superiority eliminates the need for handling hazardous solid **CA**, endowing the one-pot direct synthesis with excellent operational safety.

Single-crystal X-ray diffraction confirms that **ICA-1** belongs to the monoclinic space group $P2_1$ and exhibits an intercalation structure (**Supplementary Table 2**). The asymmetric unit contains eight Cu(II) ions, two Et_4N^+ ions, and eighteen N_3^- ions (**Supplementary Fig. 8**). Three distinct coordination modes, including square-planar, square-pyramidal, and octahedral modes, are observed for the Cu(II) centers (**Supplementary Fig. 9 and Table 3**). The crystallographically independent N_3^- ions exhibit three distinct bridging modes (**Supplementary Fig. 10**). The common μ-1,1 and rare μ_3-1,1,1 bridging N_3^- ions link adjacent Cu(II) centers to form two distinct infinite chains extending along the *a* axis (**Supplementary Figs. 11 and 12**). These chains are further interconnected by μ_3-1,1,3 and partial μ-1,1 bridging N_3^- ions, yielding an infinite $[Cu_8(N_3)_{18}]^{2-}$ energetic layer perpendicular to the *b* axis (**Fig. 1c**). The shortest nonbonding N···N contact between adjacent N_3^- ions within these energetic layers is 2.55 Å, a value comparable to that observed in **CA**, indicating that the inorganic layers retain sufficient sensitivity (**Supplementary Figs. 11, 13, and Table 4**). Two crystallographically independent Et_4N^+ cations (designated N11 and N21) pack into well-ordered organic layers parallel to the *ac* plane *via* shape complementarity. Despite the inherent electrostatic repulsion between adjacent Et_4N^+ cations, a uniform non-energetic shielding layer is well constructed with distances between adjacent methyl carbon atoms ranging from 3.82 to 4.18 Å (**Supplementary Fig. 14**). These organic layers isolate and shield adjacent energetic layers, with an intercalated distance of 12.4 Å (**Fig. 1c**). Although locally enhanced nonclassical weak

hydrogen bonds can be observed between layers, their strength remains modest (**Supplementary Table 5 and Fig. 15**), and the stable intercalated stacking is primarily attributed to strong Coulombic forces. This unique intercalated structure creates the conditions for atomically precise buffering of external non-explosive stimuli. Furthermore, experimental PXRD patterns of **ICA-1** display intense (0 2 0) and (0 4 0) reflections, corresponding to the inorganic and organic layers, respectively, while signals from other lattice planes remain extremely weak. This observation reveals a strong preferred orientation, arising from restricted crystal growth along the direction normal to the *ac* plane, consistent with the plate-like morphology of the obtained crystals (**Supplementary Fig. 16**).

Stability, safety, and mechanism

To evaluate the stability of **ICA-1**, we performed systematic aging tests in air, moisture, and intermittent light. No morphological or colour changes were observed after 60-day air exposure, 3-day moisture, and light treatments. The formation of basic copper azide impurities is fully precluded, given their inherent colour discrepancy with **ICA-1**[2]. PXRD measurements confirm the intact crystallographic purity of the treated **ICA-1** (**Fig. 2a**). Unlike pure **CA**, which spontaneously degrades into basic copper azides under ambient humid conditions, **ICA-1** possesses substantially enhanced environmental robustness. Such superior stability stems from the hydrophobic ethyl groups of intercalated Et_4N^+ cations, following a stabilization mechanism analogous to that of high-stability 2D halide perovskites[38-42].

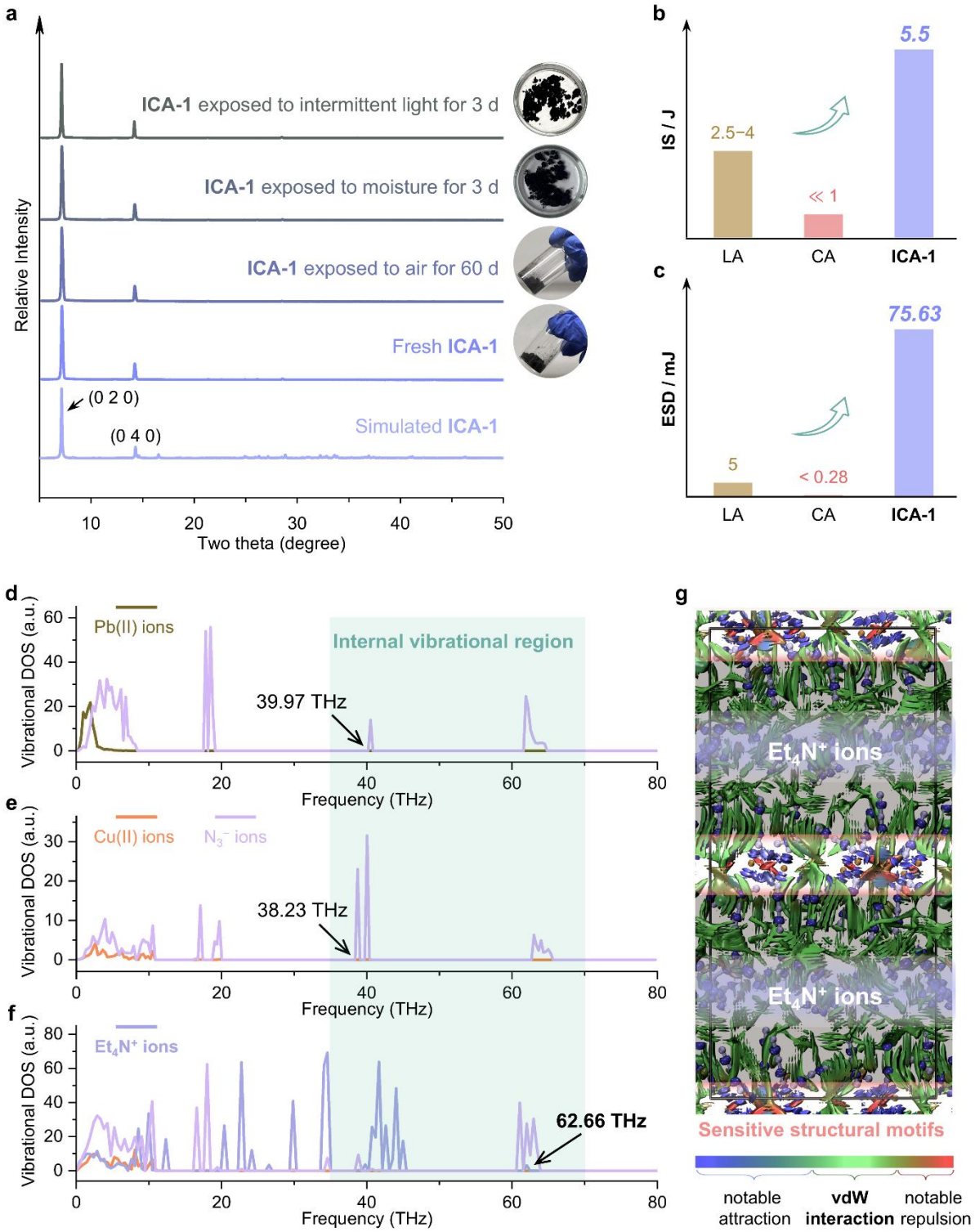

Fig. 2| Stability, safety, and theoretical calculation of ICA-1. a, PXRD patterns of **ICA-1** exposed to different environments (optical images under corresponding test conditions on the right of the test lines). **b**, The impact sensitivities of **LA**, **CA**, and **ICA-1**. **c**, The electrostatic

discharge sensitivities of **LA**, **CA**, and **ICA-1**. **d**, **e**, **f**, Vibrational density of states (**VDOS**) for **LA**, **CA**, and **ICA-1**. **g**, The interaction region indicator (**IRI**) analysis of **ICA-1**. Surface colored according to the blue-green-red (BGR) scale.

A thermal decomposition threshold over 150 °C is essential for green primary explosives for harsh-environment applications. The thermal decomposition behaviour of **ICA-1** was investigated by a blast-proof differential thermal analysis (DTA). **ICA-1** exhibits a strong exothermic peak at 204 °C with audible detonation (**Supplementary Figs. 17 and 18**), almost identical to pure **CA** (205 °C). The intercalated Et_4N^+ cations barely affect the thermal stability of the bulk. This merit endows **ICA-1** with prominent superiority over most reported nitrogen-rich compounds, satisfying practical application demands. Long-term thermal stability tests (75 °C vacuum storage for 48 h, **Supplementary Table 6**) yield a negligible mass loss (< 0.05%), demonstrating **ICA-1**'s excellent persistent thermal stability.

While the synthesis of **ICA-1** is safe, energetic materials possess intrinsic metastability toward external stimuli. It is therefore essential to define sensitivity thresholds for safe operation. According to BAM standards, **ICA-1** exhibits impact (5.5 J) and friction (5 N) sensitivities superior to those of **LA**, pure **CA**, and other **CA**-based derivatives. It also exhibits an exceptional electrostatic discharge (ESD) sensitivity of 75.63 mJ. This value is 15-fold and 270-fold higher than those of **LA** and pure **CA,** respectively (**Figs. 2b, c, and Table 1**).

To gain mechanistic insights, we analyzed the atom-projected vibrational density of states (**VDOS)** of **LA**, **CA**, and **ICA-1** using a fine-tuned machine-learning interatomic potential[43,44]. Prior studies have implicated vibrational energy transfer into azide stretching modes in the

activation of energetic azides. We therefore focus on the 35–70 THz region, which encompasses the characteristic N_3^- stretching modes most relevant to azide activation[45-48]. **Figs. 2d–f** show that **ICA-1** possesses a much denser set of low-frequency modes (below 35 THz), arising mainly from torsional and librational motions of the intercalated Et_4N^+ cations together with coupled Cu(II)–N_3^- lattice vibrations. We define the onset of the azide-only regime as the lowest frequency above which non-azide contributions become negligible within the numerical resolution and the VDOS is contributed exclusively by N_3^- modes. This onset occurs at 39.97 THz for **LA**, 38.23 THz for **CA**, and 62.66 THz for **ICA-1**. The markedly higher onset in **ICA-1** indicates that the Et_4N^+ intercalant acts as a vibrational buffer, dispersing incoming mechanical energy over non-reactive organic modes and raising the threshold of up-pumping into the N_3^- stretching range.

Like other oxygen-free nitrogen-rich energetic materials, the explosive decomposition of **ICA-1** originates primarily from the cleavage of nitrogen-containing single and double bonds. These bonds subsequently rearrange to form thermodynamically more stable N≡N triple bonds, and the energy difference between these bond types constitutes the principal source of energy release. Although the organic cations within the system also contain nitrogen atoms, statistics of decomposition products of **ICA-1** under shock at 6.8 $km \cdot s^{-1}$ reveal that N_2 formation arises predominantly from N_3^- ions. A substantial proportion of N_3^- ions transforms into N_2 on an ultrafast timescale, while only minor conversion of organic cations to N_2 occurs at a later stage. This demonstrates that N_3^- ions serve as the core contributor to energy release upon explosion (**Supplementary Fig. 19**). In this system, the Et_4N^+ layer serves as a vibrational buffer. It disperses incoming energy over non-reactive modes and lowers the probability of rapid

localization on the N_3^- ions. This interpretation is consistent with the lower mechanical sensitivity of **ICA-1**.

To visualize the nature and spatial distribution of interactions across the organic–inorganic interfaces, we performed interaction region indicator (**IRI**) analysis, which maps attractive, van der Waals, and repulsive regions from the electron density (**Fig. 2g**). The intercalated region of **ICA-1** is dominated by weak van der Waals contacts rather than a rigid extended coordination network. This weakly coupled interface limits vibrational transport between neighboring Cu–N_3^- ion sheets. At the same time, it allows the organic intercalant to dissipate part of the incoming energy before that energy reaches the N_3^- ions-centered reactive modes. The phonon and **IRI** results therefore support a common mechanism. Cation intercalant separates the energetic sheets and creates a mechanically soft intercalant that slows energy transfer into N_3^- ions bond-cleavage coordinates. We also calculated the full elastic constant tensors, as reported in **Supplementary Tables 7–9**. However, commonly used empirical descriptors[49,50] such as the Pugh ratio B/G and Cauchy pressures do not show a consistent correlation with the experimental sensitivity ordering across **LA**, **CA**, and **ICA-1**. This mismatch highlights that **ICA-1** differs from conventional energetic crystals, in which bulk elastic descriptors often provide a reasonable first estimate of sensitivity. In **ICA-1**, the hybrid layered structure shifts the controlling factor from an averaged mechanical response to local and mode-selective energy transfer across rigid Cu–N_3^- ions sheets and soft organic intercalants.

Table 1. Properties of **ICA-1** and selected primary explosives.

Compound	ρ^{a} (g·cm^{-3})	$T_{dec}{}^{b}$ (°C)	N^{c} (%)	IS^{d} (J)	FS^{e} (N)	ESD^{f} (mJ)
ICA-1	1.989	204	51.43	5.5	5	75.63
LA	4.800	315	28.9	2.5−4	0.1−1	5
CA[30]	2.60	205	56.9	≪ 1	≪ 0.1	< 0.28
MOFT-CA[15]	2.2	204	43.10	1	5	1.6
Cu-MTZ[30]	2.036	148	60.46	< 1	< 0.1	0.79
K_2DNABT[50]	2.11	200	50.28	1	≤ 1	3
K_2DNAT[19]	2.18	240	42.08	1	< 5	–
ICM-103[12]	1.86	160.3	56.50	4	60	130
DPPE-1[25]	2.88	161.3	4.95	3.5	5.0	–

[a] Crystal density.

[b] Decomposition temperature.

[c] Nitrogen content.

[d] Impact sensitivity.

[e] Friction sensitivity.

[f] Electrostatic discharge sensitivity.

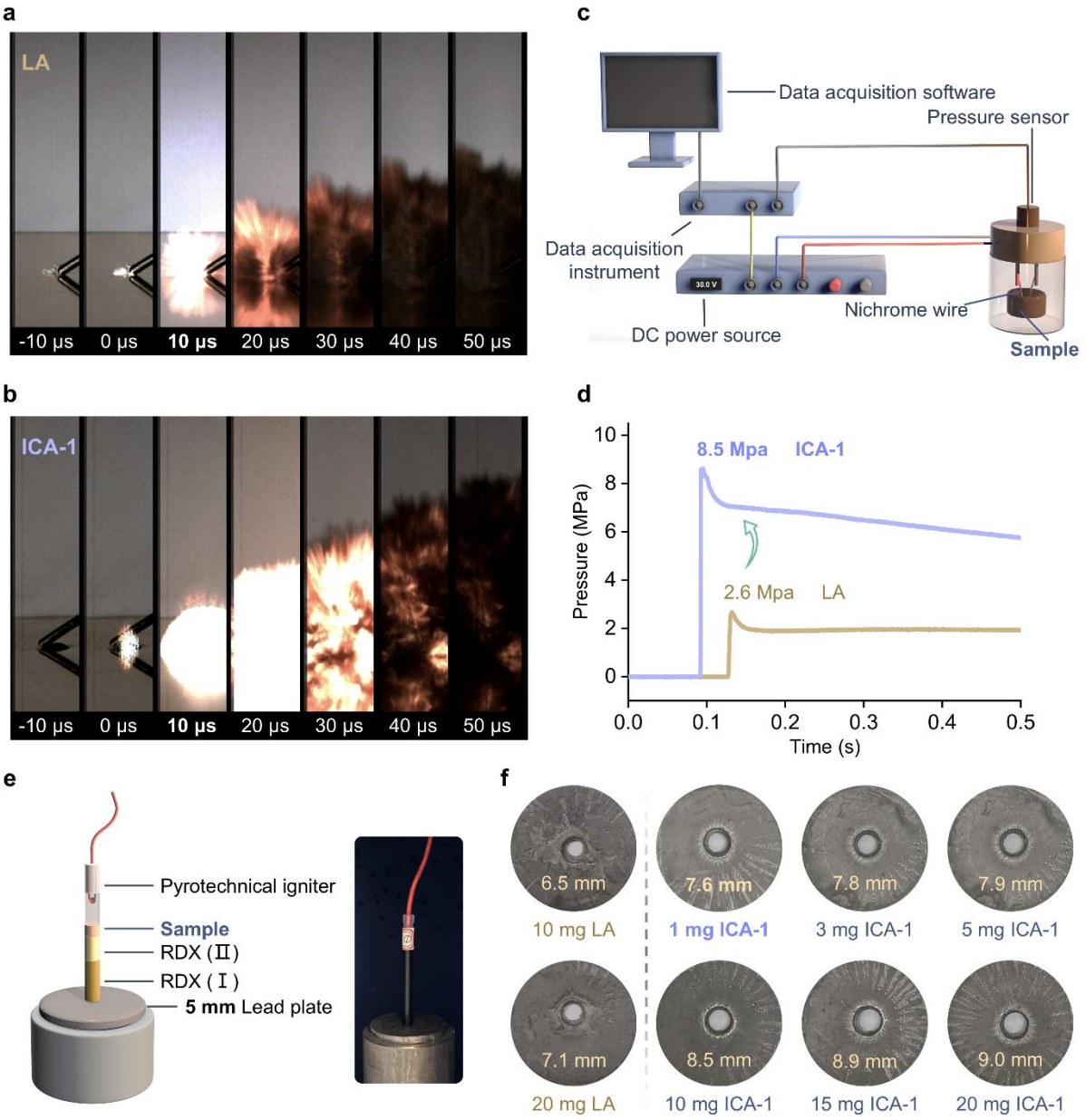

Fig. 3|Evaluation of the initiating ability of ICA-1. a, **b**, Hot needle experiment of **LA** (top) and **ICA-1** (bottom). **c**, Schematic of sealed-chamber explosion test setup. **d**, Time-pressure curves of **LA** and **ICA-1**. **e**, Minimum primary charge (MPC) test apparatus. **f**, Damage to 5 mm-thick lead plate by detonation of detonators with different dosages of **LA** and **ICA-1** as initiating charges.

Initiation efficiency

Primary explosives operate by rapidly producing detonation waves, with DDT capacity and detonation output as core performance metrics. Hot-needle tests (**Figs. 3a and b**) at 100000 frames per second (fps) reveal that **ICA-1** achieved ultra-fast DDT within 10 μs, comparable to conventional **LA**. **ICA-1** generated a larger detonation fireball owing to its higher nitrogen content. Flame and hot-plate tests further validate its prominent DDT performance (**Supplementary Figs. 20 and 21**).

ICA-1 cannot undergo stable combustion, preventing enthalpy measurement *via* oxygen bomb calorimetry and theoretical detonation parameter calculation. We thus evaluated its energetic performance against **LA** (the military benchmark primary explosive) *via* sealed-chamber explosion tests. Samples were ignited by a 30 V DC-powered nichrome wire, and time-pressure curves were recorded. **ICA-1** delivers a peak explosion pressure of 8.5 MPa, 3.3 times that of LA (2.6 MPa) under identical conditions (**Figs. 3c and d**).

Owing to the multifactorial nature of explosive energy release, we adopted a 2-mm-thick lead-plate perforation test to further evaluate detonation performance. Under identical conditions in stainless-steel sleeves with commercial ignition, **ICA-1** yielded a perforation diameter of 16.7 mm, 1.3 times that of **LA** (13.0 mm) (**Supplementary Fig. 22**). Combining time-pressure curves and perforation results, **ICA-1** delivers detonation output superior to that of **LA**. Its fast DDT capacity and high detonation output validate its significant potential as a high-performance primary explosive.

Initiating efficiency serves as the principal metric for primary explosive evaluation, which is quantified by the minimum primary charge (MPC) capable of triggering detonation of

secondary explosives (e.g., cyclotrimethylenetrinitramine, RDX). Systematic MPC tests of **ICA-1** verified its reliable RDX initiation at an extremely low dosage of 1 mg, which yielded a 7.6 mm lead-plate perforation diameter, exceeding the 7.0 mm outer diameter of detonator shells. Moreover, 20 mg **ICA-1** generated a perforation diameter of 9.0 mm, distinctly superior to 7.1 mm for equivalent **LA** loading. These results reveal the MPC as low as 1 mg for **ICA-1** under our experimental conditions (pressing pressure: 14.7 MPa). By contrast, **LA** exhibits an MPC value of 20 mg under the same pressing pressure, highlighting differences in optimal pressing pressures among primary explosives. Furthermore, prior literature reports an MPC of 10 mg for **LA** at higher pressing pressures[12,22], establishing that **ICA-1** possesses at least 10-fold greater initiation capability than **LA** and highlighting its notable potential for next-generation green primary explosives. (**Figs. 3e and f, and Supplementary Fig. 23**).

Chip-scale initiation

Conventional tripartite explosive trains (ignition powder, primary explosive, and secondary explosive) are limited by excessive volume, hindering the miniaturization of aerospace components, high-voltage quick-break pyrotechnic fuses, and related devices, which renders chip-scale initiation a preferable engineering technical route. These chip-scale energetic devices employ semiconductor-bridge thin films for electrothermal transduction, outperforming traditional metallic bridges in both size and thermal response speed. Under such extremely confined charging conditions, the ignition powder is eliminated, and the semiconductor-bridge film must directly initiate detonation of the primary explosive, which in turn triggers the secondary explosive. However, semiconductor-bridge thin films provide

insufficient heat for direct initiation of conventional primary explosives. Accordingly, eligible primary explosives should possess a low input ignition energy, high initiation efficiency, robust stability, intrinsic safety, favorable environmental compatibility, and satisfactory cost-effectiveness.

Plastic sample cups containing **LA** or **ICA-1** were mounted onto commercial bridgewire electroigniters (devoid of ignition powder). Varying input voltages were applied to assess the critical input ignition energy and thermal response of the two materials. As shown in **Figs. 4a-d and Supplementary Tables 10 and 11**, **ICA-1** enables reliable ignition at an input voltage of only 2 V with a 20.97 ms delay, whereas **LA** cannot be ignited under identical conditions. **LA** achieves ignition at 2.5 V (19.07 ms delay), while **ICA-1** shortens the delay to 11.59 ms at the same voltage, corresponding to a 40% faster response. These data verify that **ICA-1** possesses lower critical input ignition energy and superior thermal response relative to **LA**. Benefiting from the excellent initiation performance, **ICA-1** is promising for chip-scale initiation systems (**Supplementary Figs. 24 and 25**).

Given these superior comprehensive properties, **ICA-1** was further verified as a primary explosive for chip-scale initiation systems. The PCB-based microchip integrated a 1 mm-diameter charge cavity loaded with 0.8 mg of **LA** or **ICA-1** (**Fig. 4e**). Assembled in a stainless-steel mould with 10 mg hexanitrohexaazaisowurtzitane (CL-20), the device forms a complete chip-scale explosive train initiated by a semiconductor bridge. Distinct craters on aluminum targets confirm that **ICA-1** reliably triggers CL-20 detonation at the microscale (**Fig. 4f and Supplementary Fig. 26**). Notably, **ICA-1** delivers robust initiation efficiency without auxiliary ignition powder, validating its substantial potential for miniaturized initiation cores.

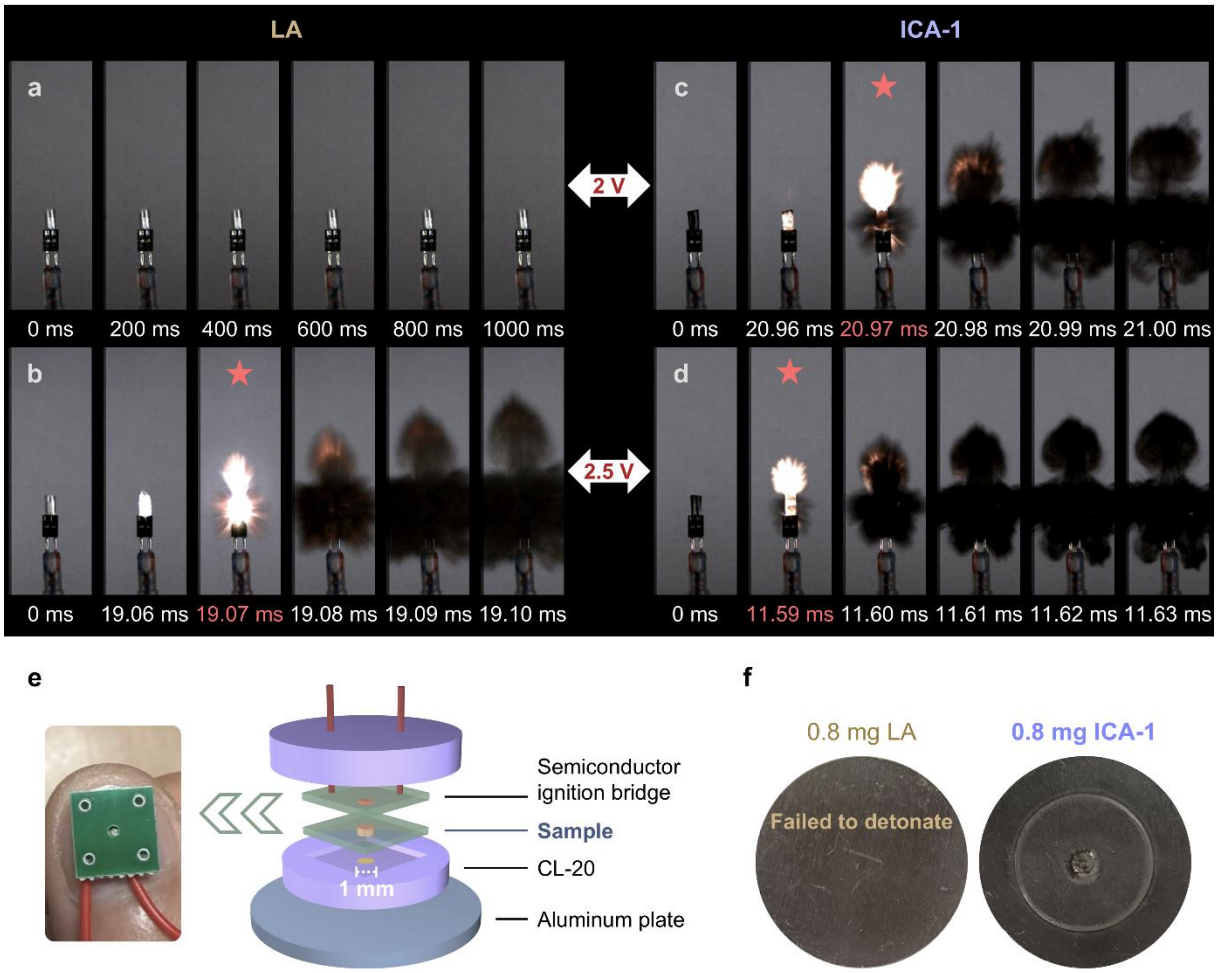

Fig. 4|Input ignition energy evaluation and application potential of ICA-1 in chip-scale initiation systems. a, **LA** with input voltage of 2 V. **b**, **LA** with input voltage of 2.5 V. **c**, **ICA-1** with input voltage of 2 V. **d**, **ICA-1** with input voltage of 2.5 V. **e**, Schematic diagram of the chip-scale initiation systems. **f**, Damage effects on aluminum plates by detonation of **LA** and **ICA-1**-loaded energetic chips.

Conclusion

This work establishes a new paradigm (**ICA**) for primary explosives, delivering a transformative route to resolve the century-old trade-off among stability, safety, environmental compatibility, initiation efficiency, and cost-effectiveness that plagues conventional **LA**.

Integrating crystal and energetic chemistry, the cation-intercalation strategy overcomes the inherent technical limitations of traditional energetic systems and achieves superiority over conventional **LA** in core performance metrics, offering a viable pathway toward advanced chip-scale initiation technologies for aerospace and pyrotechnic safety devices. The rationally engineered alternating non-energetic layer and energetic layer stacking intercalated structure retains superior initiation efficiency alongside drastically reduced sensitivity (IS = 5.5 J; ESD = 75.63 mJ). Facile high-yield (79%) aqueous synthesis from affordable industrial feedstocks removes cost and scale-up bottlenecks for practical **LA** substitution. Mechanistically, the intercalated cations impede phonon up-pumping, spatially isolate energetic copper–azide layers, and inhibit the generation of hot spots, thereby establishing a potentially transferable desensitization mechanism with low energy loss for energetic materials. We anticipate that this work will drive transformative progress in energetic materials and inspire in-depth interdisciplinary integration across supramolecular, inorganic, and materials chemistry.

References

1. Giles, J. Green explosives: collateral damage. *Nature* **427**, 580–581 (2004).
2. Matyáš, R. & Pachman, J. *Primary Explosives* (Springer, 2013).
3. Huynh, M. H. V., Coburn, M. D., Meyer, T. J. & Wetzler, M. Green primary explosives: 5-nitrotetrazolato-N^2-ferrate hierarchies. *Proc. Natl. Acad. Sci. U. S. A*. **103**, 10322–10327 (2006).
4. Huynh, M. H. V., Hiskey, M. A., Meyer, T. J. & Wetzler, M. Green primaries: Environmentally friendly energetic complexes. *Proc. Natl. Acad. Sci. U. S. A*. **103**, 5409–5412 (2006).
5. Ricciardulli, A. G., Yang, S., Smet, J. H. & Saliba, M. Emerging perovskite monolayers. *Nat. Mater.* **20**, 1325–1336 (2021).
6. Liu, C. et al. Two-dimensional perovskitoids enhance stability in perovskite solar cells. *Nature* **633**, 359–364 (2024).
7. Fronabarger, J. W. et al. DBX-1 – a lead-free replacement for lead azide. *Propell. Explos. Pyrot.* **36**, 541–550 (2011).
8. Shang, Y. et al. Silver(I)-based molecular perovskite energetic compounds with exceptional thermal stability and energetic performance. *Inorg. Chem.* **61**, 4143–4149 (2022).
9. Fang, Z. X., Wang, C., Wei, Y. L., Wang, Q. Y. & Zang, S. Q. Constructing highly reliable and adaptive primary explosive composites for micro-initiator assisting by a hybrid template of metal–organic frameworks and cross-linked polymers. *Small* **19**, 2300157 (2023).
10. Xu, J.-G. et al. Coordination polymerization of metal azides and powerful nitrogen-rich ligand toward primary explosives with excellent energetic performances. *Chem. Mater.* **29**, 9725–9733 (2017).
11. Wang, T. et al. Evolution of oxidizing inorganic metal salts: Ultrafast laser initiation materials based on energetic cationic coordination polymers. *ACS Appl. Mater. Interfaces* **11**, 41523–41530 (2019).
12. Deng, M., Feng, Y., Zhang, W., Qi, X. & Zhang, Q. A green metal-free fused-ring initiating substance. *Nat. Commun.* **10**, 1339 (2019).
13. Hu, W. et al. An efficient one-step reaction for the preparation of advanced fused bistetrazole-based primary explosives. *ACS Cent. Sci.* **9**, 742–747 (2023).
14. Cui, M. et al. Structure-induced energetic coordination compounds as additives for laser initiation primary explosives. *Adv. Mater.* **37**, 2414886 (2024).
15. Wang, Q. et al. Metal-organic framework templated synthesis of copper azide as the primary explosive with low electrostatic sensitivity and excellent initiation ability. *Adv. Mater.* **28**, 5837–5843 (2016).
16. Sun, Q., Li, X., Lin, Q. & Lu, M. Dancing with 5-substituted monotetrazoles, oxygen-rich ions, and silver: towards primary explosives with positive oxygen balance and excellent energetic performance. *J. Mater. Chem. A* **7**, 4611–4618 (2019).
17. Lei, G. et al. A three-dimensional energetic coordination compound (BLG-1) with excellent initiating ability for lead-free primary explosives. *Mater. Horiz.* **10**, 5775–5781 (2023).

18. Lv, R. et al. Host–Guest Synergy of Metal–organic frameworks for enhanced near-infrared ultrafast laser responsiveness. *ACS Cent. Sci.* **11**, 583–591 (2025).
19. Fischer, D., Klapötke, T. M. & Stierstorfer, J. 1,5-Di(nitramino)tetrazole: High sensitivity and superior explosive performance. *Angew. Chem. Int. Ed.* **54**, 10299–10302 (2015).
20. He, C. & Shreeve, J. M. Potassium 4,5-Bis(dinitromethyl)furoxanate: A green primary explosive with a positive oxygen balance. *Angew. Chem. Int. Ed.* **55**, 772–775 (2016).
21. Huang, W., Tang, Y., Imler, G. H., Parrish, D. A. & Shreeve, J. M. Nitrogen-rich tetrazolo[1,5-b]pyridazine: Promising building block for advanced energetic materials. *J. Am. Chem. Soc.* **142**, 3652–3657 (2020).
22. Yu, Q., Zheng, Z., Yi, Z., Yi, W. & Shreeve, J. M. Exploring the maximum potential of initiating ability in metal-free primary explosives. *J. Am. Chem. Soc.* **147**, 5125–5131 (2025).
23. Benz, M., Klapötke, T. M., Krumm, B., Lommel, M. & Stierstorfer, J. Nitrocarbamoyl azide $O_2NN(H)C(O)N_3$: A stable but highly energetic member of the carbonyl azide family. *J. Am. Chem. Soc.* **143**, 1323–1327 (2021).
24. Wurzenberger, M. H. H., Szimhardt, N. & Stierstorfer, J. Copper(II) chlorate complexes: The renaissance of a forgotten and misjudged energetic anion. *J. Am. Chem. Soc.* **140**, 3206–3209 (2018).
25. Feng, Y., Zhang, J., Cao, W., Zhang, J. & Shreeve, J. M. A promising perovskite primary explosive. *Nat. Commun.* **14**, 7765 (2023).
26. Yu, Z.-H. et al. Periodate-based molecular perovskites as promising energetic biocidal agents. *Sci. China Mater.* **66**, 1641–1648 (2022).
27. Chen, S. et al. Periodate-based perovskite energetic materials: A strategy for high-energy primary explosives. *Small* **19**, 2302631 (2023).
28. Wang, C. et al. Core-shell hetero-framework derived copper azide composites as excellent laser-ignitable primary explosives. *Adv. Funct. Mater.* **32**, 2207524 (2022).
29. Pelletier, V. et al. Copper Azide Confined Inside Templated Carbon Nanotubes. *Adv. Funct. Mater.* **20**, 3168–3174 (2010).
30. Wurzenberger, M. H. H., Lommel, M., Gruhne, M. S., Szimhardt, N. & Stierstorfer, J. Refinement of copper(II) azide with 1-alkyl-5H-tetrazoles: Adaptable energetic complexes. *Angew. Chem. Int. Ed.* **59**, 12367–12370 (2020).
31. Kofen, M., Lommel, M., Wurzenberger, M. H. H., Klapötke, T. M. & Stierstorfer, J. 1-(Azidomethyl)-5H-Tetrazole: A powerful new ligand for highly energetic coordination compounds. *Chem. Eur. J.* **28**, e202200492 (2022).
32. Yan, Y.-F. et al. Sensitive structural motifs separately distributed in azide-based 3D EMOFs: a primary explosive with an excellent initiation ability and enhanced stability. *Inorg. Chem. Front.* **9**, 5884–5892 (2022).
33. Yan, Y.-F. et al. Copper azide-based complexes without repulsive steric clashes between azides for advanced primary explosives. *Chem. Eng. J.* **472**, 144982 (2023).
34. Zhang, J., Mitchell, L. A., Parrish, D. A. & Shreeve, J. M. Enforced layer-by-layer stacking of energetic salts towards high-performance insensitive energetic materials. *J. Am. Chem. Soc.* **137**, 10532–10535 (2015).
35. Wang, Y. et al. Accelerating the discovery of insensitive high-energy-density materials

by a materials genome approach. *Nat. Commun.* **9**, 2444 (2018).
36. Zhang, J. et al. One step closer to an ideal insensitive energetic molecule: 3,5-Diamino-6-hydroxy-2-oxide-4-nitropyrimidone and its derivatives. *J. Am. Chem. Soc.* **143**, 12665–12674 (2021).
37. Yu, C.-X., Ye, L., Zhuo, H., Yan, Y.-F. & Zhang, W.-X. Barium(II)-based molecular perovskite energetic compounds for next-generation pyrotechnic materials. *Inorg. Chem. Front.* **12**, 4645–4652 (2025).
38. Xu, Z. et al. Precisely tailoring a $FAPbI_3$-derived ferroelectric for sensitive self-driven broad-spectrum polarized photodetection. *J. Am. Chem. Soc.* **145**, 1524–1529 (2023).
39. Wu, Z. et al. Alloying *n*-butylamine into $CsPbBr_3$ to give a two-dimensional bilayered perovskite ferroelectric material. *Angew. Chem. Int. Ed.* **57**, 8140–8143 (2018).
40. Mao, L., Stoumpos, C. C. & Kanatzidis, M. G. Two-dimensional hybrid halide perovskites: Principles and promises. *J. Am. Chem. Soc.* **141**, 1171–1190 (2018).
41. Liu, Y. et al. 0D Pyramid-intercalated 2D bimetallic halides with tunable electronic structures and enhanced emission under pressure. *Angew. Chem. Int. Ed.* **62**, e202314977 (2023).
42. Song, Y. et al. Structure–emission property relationship of bilayer 2D hybrid perovskites. *J. Am. Chem. Soc.* **147**, 19902–19910 (2025).
43. Zhang, D. et al. A graph neural network for the era of large atomistic models. *npj Comput. Mater.* **12**, 2146 (2026).
44. Guo, M.-Y. et al. DeepEMs-25: a deep-learning potential to decipher kinetic tug-of-war dictating thermal stability in energetic materials. *npj Comput. Mater.* **11**, 246 (2025).
45. Michalchuk, A. A. L. et al. Predicting the reactivity of energetic materials: an ab initio multi-phonon approach. *J. Mater. Chem. A* **7**, 19539–19553 (2019).
46. Qian, W. & Zhang. C. Review of the phonon calculations for energetic crystals and their applications. *Energ. Mater. Front.* **2**, 154–164 (2021).
47. Diana, E., Gatterer, K. & Kettle, S. F. A. The vibrational spectroscopy of the coordinated azide anion; a theoretical study. *Phys. Chem. Chem. Phys.* **18**, 414–425 (2016).
48. Michalchuk, A. A. L., Fincham, P. T., Portius, P., Pulham, C. R. & Morrison, C. A. A. pathway to the athermal impact initiation of energetic azides. *J. Phys. Chem. C* **122**, 19395–19408 (2018).
49. Pugh, S. F. Relations between the elastic moduli and the plastic properties of polycrystalline pure metals. *Philos. Mag.* **45**, 823–843 (1954).
50. Pettifor, D. G. Theoretical predictions of structure and related properties of intermetallics. *Mater. Sci. Technol.* **8**, 345–349 (1992).
51. Fischer, D., Klapötke, T. M. & Stierstorfer, J. Potassium 1,1′-Dinitramino-5,5′-bistetrazolate: A primary explosive with fast detonation and high initiation power. *Angew. Chem. Int. Ed.* **53**, 8172–8175 (2014).

Methods

Caution!

Sodium azide, **LA**, **CA**, **ICA-1**, RDX, and CL-20 are explosive substances. Operators must wear appropriate protective equipment at all times during experimentation, including bulletproof vests, Kevlar helmets fitted with bulletproof face shields, and Kevlar gloves. These compounds must under no circumstances be exposed to any form of mechanical stimuli, such as impact, friction, or static sparks.

General methods

Thermal decomposition behaviours of the samples were characterised *via* differential thermal analysis (DTA) using an OZM Research DTA 552-Ex instrument with a linear heating rate of 5 °C·min^{-1}, spanning from room temperature to 500 °C. PXRD patterns (Cu *K*α radiation) were acquired on a Bruker Advance D8 diffractometer. Simulated diffraction patterns were generated using Mercury software (version 2020) based on single-crystal structural data. Mechanical sensitivities were measured using a BAM fall hammer BFH-12 and a BAM friction apparatus FSKM-10. Electrostatic discharge (ESD) sensitivity was tested with an OZM Research Xspark8 electrostatic spark sensitivity meter. A SH6-116 high-speed camera (SinceVision Technology Co., Ltd., Shenzhen, China) was utilised to record the entire procedures of hot needle tests and input ignition energy evaluation tests. Chip-scale initiation tests were recorded using a Phantom VEO 610L high-speed camera.

Materials and synthesis

All the reagents are commercially available and used directly for synthesis without further purification. Tetraethylammonium chloride (98.0%) and copper(II) nitrate (98.0%) were purchased from Shanghai Macklin Biochemical Technology Co., Ltd. Sodium azide (≥ 99.0%) was purchased from Sinopharm Chemical Reagent Co., Ltd.

Synthesis of $(Et_4N)_2[Cu_8(N_3)_{18}]$ (ICA-1).

Direct synthesis:

Tetraethylammonium chloride (331.4 mg, 2 mmol) and sodium azide (1170.2 mg, 18 mmol) were dissolved in 30 mL water to form a clear solution. Then, 10 mL copper(II) nitrate (1500.4 mg, 8 mmol) solution was added to the reaction system while stirring, and the precipitate formed almost immediately. After a few minutes, the precipitate was collected by vacuum filtration. The filter cake was washed with 10 mL of ethanol and subsequently dried at room temperature. Yield: 79% (based on copper(II) nitrate). Anal. Calcd for $C_{16}H_{40}N_{56}Cu_8$: C 12.60, H 2.64, N 51.43%. Found: C 12.92, H 2.73, N 51.23%. IR (KBr, cm^{-1}): 2988 w, 2834 w, 2122 s, 2039 s, 1486 w, 1394 w, 1359 w, 1278 s, 1171 w, 1000 w, 781 w, 683 w, 582 w (**Supplementary Fig. 6**).

Indirect synthesis:

0.5 mL aqueous solution of copper(II) nitrate (150.0 mg, 0.8 mmol) was slowly added to 2.5 mL aqueous solution of sodium azide (104.0 mg, 1.6 mmol), affording a copper azide suspension. Tetraethylammonium chloride (33.1 mg, 0.2 mmol) and sodium azide (13.0 mg,

0.2 mmol) were dissolved in 1 mL of deionized water, yielding a clear aqueous solution. Upon gentle mixing of the two aforementioned mixtures, the resultant mixture was subjected to ultrasonic treatment for 30 min, and the target product **ICA-1** was obtained. Yield: 79.3% (based on copper(II) nitrate).

Single-crystal X-ray crystallography

Single-crystal X-ray diffraction data were collected on a Rigaku diffractometer (CrysAlisPro 1.171.42.90a (Rigaku OD, 2023)) with graphite-monochromated Cu *K*α radiation (λ = 1.54184 Å). The structures were solved with direct methods and refined with a full-matrix least-squares technique with the SHELXTL software package. Anisotropic thermal parameters were applied to all non-hydrogen atoms, and the hydrogen atoms were generated geometrically.

Sensitivity tests

The BAM fall hammer measured the impact sensitivity of **ICA-1** according to STANAG 4489 (OZM Research). Friction sensitivity was determined based on STANAG 4487 using a FSKM-10 BAM friction device (manufactured by OZM Research). The ESD value of the sample was tested using the OZM research Xpark8 electrostatic spark sensitivity meter, and the discharge energy was obtained based on the formula $E = 0.5\ CU^2$. C represents the capacitance of the capacitor in farads (F) and U represents the charging voltage in volts (V).

Hot needle tests

The sample (30 mg) was loosely spread on a 1-mm-thick brass plate. A metal needle

heated to red heat by a Bunsen burner was used to contact the sample, and the corresponding response of the sample was observed. The experiment was recorded at a frame rate of 100000 frames per second.

Sealed-chamber explosion tests

40 mg of the sample was loaded into a quartz crucible. The nichrome wire connected to the electrodes was adjusted to make contact with the sample. Subsequently, the sample was ignited by a 30 V DC power source in a sealed tank. Meanwhile, the dynamic pressure changes inside the tank were captured by a pressure sensor and transmitted to a dedicated software for processing to obtain the time−pressure curves.

Minimum primary charge (MPC) tests

First, 450 mg of RDX (I) was pressed into a 0.2-mm-thick detonator shell under a pressure of 40 MPa. Subsequently, 220 mg of RDX (II) was pressed into the detonator shell under a certain pressure (P). Finally, a certain amount of primary explosive (either **ICA** compound or **LA**) was pressed into the aforementioned detonator shell pre-loaded with RDX under the same pressure (P), followed by the assembly of an electric initiator. The test detonator was placed on a 5-mm-thick lead plate and initiated. By adjusting the charge mass of the primary explosive and the charging pressure (P), the critical mass (minimum primary charge, MPC) and charging pressure (P) that enable the test detonator to completely perforate the lead plate were determined.

In each test, 450 mg of RDX was pressed into an industrial detonator shell with 0.2 mm thickness at 40 MPa. A further 220 mg of RDX and a measured amount of primary explosive

were then sequentially pressed into the shell at 14.7 MPa. The loaded shell was assembled with a standard pyrotechnic igniter to form a test detonator.

Input ignition energy evaluation tests

A plastic sample cup was mounted on a commercial bridgewire electroigniter, and approximately 30 mg of the sample was loosely loaded into the cup. A 47 μF capacitor was charged using a DC power supply and then connected to the aforementioned bridgewire electroigniter to form a discharge circuit. The heat output of the bridgewire was controlled by varying the charging voltage of the capacitor. The ignition event and the corresponding ignition delay time were recorded. A high-speed camera operating at 100000 frames per second was synchronized with the igniter to capture the entire experimental process.

Chip-scale initiation tests

The primary explosive and CL-20 were gently pressed into the corresponding charge holes, respectively. The test device was assembled according to the charge structure shown in **Fig. 4e**. It was then initiated using a 30 V DC power supply. The ignition event was recorded with a high-speed camera operating at 5000 frames per second.

Theoretical calculation

Machine learning interatomic potential.

All atomistic simulations in this work employ a machine learning interatomic potential (MLIP) based on the DPA3 architecture[43] with a repflow descriptor ($n_{\mathrm{dim}} = 256$, $e_{\mathrm{dim}} = 128$, a_{dim}

= 32), 3 message-passing layers, an energy cutoff radius of 6.0 Å, and an angular cutoff radius of 4.0 Å. The fitting network consists of three hidden layers of width 240 with residual connections and SiLU activation. The pretrained model was trained on the DeepEMs-25 dataset[44] and was then fine-tuned on a domain-specific dataset for the CA-series systems. Fine-tuning used the same DPA3 architecture and was performed for 10^6 gradient steps with a batch size of auto:512. The learning rate decayed exponentially from 10^{-3} to 10^{-5}. The loss function weighted energy, force, and virial contributions with prefactors decaying from (0.2, 1000, 0.02) to (20, 20, 1), progressively shifting emphasis from forces to energies and virials. The fine-tuning dataset includes NVT molecular dynamics at 200–4000 K, NPT runs under uniaxial, biaxial, triaxial, and tilted-triaxial strain conditions, and high-pressure decomposition trajectories up to 120 GPa. Validation was performed on held-out trajectories of the same types. The converged validation RMSE values, averaged over the final 1000 logged steps, are 2.0 meV atom^{-1} for energy, 0.15 eV Å^{-1} for forces, and 5.8 meV atom^{-1} for virials.

Phonon dispersion and vibrational density of states.

Phonon calculations were performed using the finite-displacement supercell method as implemented in Phonopy[52]. The experimental crystal structures of **LA** (ICSD 1298)[53], **CA** (ICSD 24340)[54], and **ICA-1** (this work) were fully relaxed (atomic positions and cell parameters) with a force convergence threshold of 5 meV Å^{-1} using the ASE library[55]. Supercell dimensions were chosen to exceed 40 Å in each direction: **LA**, 6 × 2 × 3; **CA**, 2 × 12 × 4; **ICA-1**, 4 × 1 × 3. Atomic displacements of 0.01 Å were applied. Interatomic forces on all displaced supercells were evaluated with the MLIP. Phonon band structures were computed along high-symmetry paths determined by SeeK-path[56]. Projected densities of states (PDOS) were computed on a Γ-

centred mesh with Gaussian smearing $\sigma = 0.01$ THz.

Elastic constant calculation.

The full second-order elastic constant tensor C_{ij} (Voigt notation) was determined by the stress–strain method[57] using the same MLIP. Each crystal structure was relaxed to a force below 10 meV Å^{-1} using the FIRE optimiser. Six independent strain states (three normal and three shear) were applied at four amplitudes in the range [−0.01, +0.01]. At each strained configuration, atomic positions were relaxed at fixed cell shape, and the Cauchy stress tensor was evaluated. Elastic constants were extracted by linear regression of stress versus strain using Pymatgen[58]. Polycrystalline averages were computed by the Voigt–Reuss–Hill (VRH) scheme[59]. Specifically, the Voigt bulk and shear moduli are given by $B_V = (C_{11} + C_{22} + C_{33} + 2(C_{12} + C_{13} + C_{23}))/9$ and $G_V = (C_{11} + C_{22} + C_{33} - C_{12} - C_{13} - C_{23} + 3(C_{44} + C_{55} + C_{66}))/15$. Using the compliance tensor $S_{ij} = C_{ij}^{-1}$, the Reuss bulk and shear moduli are $B_R = 1/(S_{11} + S_{22} + S_{33} + 2(S_{12} + S_{13} + S_{23}))$ and $G_R = 15/[4(S_{11} + S_{22} + S_{33}) - 4(S_{12} + S_{13} + S_{23}) + 3(S_{44} + S_{55} + S_{66})]$. The Hill averages are then $B_H = (B_V + B_R)/2$ and $G_H = (G_V + G_R)/2$. Young's modulus and Poisson's ratio were obtained from $E = 9B_HG_H/(3B_H + G_H)$ and $\nu = (3B_H - 2G_H)/(2(3B_H + G_H))$. The universal elastic anisotropy index was computed as $A^U = 5G_V/G_R + B_V/B_R - 6$. Cauchy pressures were computed as $C_{12} - C_{66}$, $C_{13} - C_{55}$, and $C_{23} - C_{44}$[49].

Interaction region indicator (IRI) analysis.

The periodic electron densities of compounds were obtained from single-point DFT calculations using CP2K (version 2023.1) with the PBE functional[60], DZVP-MOLOPT-SR-GTH basis sets, and GTH pseudopotentials. A plane-wave cutoff of 600 Ry was used with Γ-point sampling. The converged electron densities were exported as Gaussian cube files. The IRI

scalar field and the sign(λ_2)ρ-coloured isosurface were computed using Multiwfn (version 3.8)[61]. The IRI isosurfaces (isovalue = 1.0) were rendered in VMD with a blue–green–red colour scale mapped to sign(λ_2)ρ, where blue denotes notable attraction, green denotes van der Waals interaction, and red denotes notable repulsion.

Multiscale shock technique simulations.

Shock compression of **ICA-1** was simulated using the multiscale shock technique (MSST) implemented in LAMMPS[62,63]. Interatomic energies and forces were evaluated using with the DPA1-L0 descriptor. The experimental unit cell was replicated 4 × 3 × 3 along the crystallographic *a*, *b*, and *c* axes, respectively. The supercell was energy-minimized and equilibrated at 300 K and 1 bar for 20 ps in the NPT ensemble with a 1 fs timestep. A shock was then applied along the crystallographic *b* direction at 6.8 km·s^{-1} using an MSST cell-mass parameter of 100 (g·mol^{-1})^2·Å^{-4} and a 0.1 fs timestep. Molecular species were identified from the trajectory using ReacNetGenerator[64] with ASE-based bond perception, excluded Cu–N connectivity. Each N_2 molecule was assigned an azide, organic-cation, or mixed origin according to the timestep-zero identities of its constituent nitrogen atoms. The source-resolved fractions in **Supplementary Fig. 19b** were normalized by the initial numbers of nitrogen atoms in the azide and organic-cation populations.

References

52. Togo, A., Tanaka, I. First principles phonon calculations in materials science. *Scr. Mater.* **108**, 1–5 (2015).
53. Megaw, H. D. Crystal structure of lead azide. *Nature* **134**, 900 (1934).
54. Agrell, I. The Crystal Structure of $Cu(N_3)_2$. *Acta Chem. Scand.* **21**, 2647–2658 (1967).
55. Larsen, A. H. et al. The atomic simulation environment—a Python library for working with atoms. *J. Phys.: Condens. Matter* **29**, 273002 (2017).

56. Hinuma, Y., Pizzi, G., Kumagai, Y., Oba, F. & Tanaka, I. Band structure diagram paths based on crystallography. *Comput. Mater. Sci.* **128**, 140–184 (2017).
57. Nielsen, O. H. & Martin, R. M. First-principles calculation of stress. *Phys. Rev. Lett.* **50**, 697–700 (1983).
58. Ong, S. P. et al. Python Materials Genomics (pymatgen): A robust, open-source python library for materials analysis. *Comput. Mater. Sci.* **68**, 314–319 (2013).
59. Hill, R. The elastic behaviour of a crystalline aggregate. *Proc. Phys. Soc. A* **65**, 349–354 (1952).
60. Perdew, J. P., Burke, K. & Ernzerhof, M. Generalized gradient approximation made simple. *Phys. Rev. Lett.* **77**, 3865–3868 (1996).
61. Lu, T. & Chen, F. Multiwfn: A multifunctional wavefunction analyzer. *J. Comput. Chem.* **33**, 580–592 (2012).
62. Thompson, A. P. et al. LAMMPS–a flexible simulation tool for particle-based materials modeling at the atomic, meso, and continuum scales. *Comput. Phys. Commun.* **271**, 108171 (2022).
63. Reed, E. J., Fried, L. E. & Joannopoulos, J. D. A method for tractable dynamical studies of single and double shock compression. *Phys. Rev. Lett.* **90**, 235503 (2003).
64. Zeng, J. et al. ReacNetGenerator: an automatic reaction network generator for reactive molecular dynamics simulations. *Phys. Chem. Chem. Phys.* **22**, 683–691 (2020).

Data availability

CCDC 2558505 contains supplementary crystallographic data for this paper. These data can be obtained free of charge via www.ccdc.cam.ac.uk/data_request/cif, or by emailing data_request@ccdc. cam.ac.uk, or by contacting The Cambridge Crystallographic Data Centre, 12 Union Road, Cambridge CB2 1EZ, UK; fax: +44 1223 336033. All data supporting this work are fully available within the paper and accompanying supplementary resources.

Acknowledgements

This work was supported by National Natural Science Foundation of China (22625508, U2341287, and 22488101) and Guangzhou Science and Technology Program (2024A04J6499).

Author contributions

Y.-F. Yan conceptualized, designed, and performed the major experiments and corresponding data analysis. W.-X. Zhang provided key guidance for the conception and design of this study. M.-Y. Guo provided support for theoretical calculations and result analyses. Q.-Y. Wang and X.-Y. Wang provided key assistance with the chip-scale initiation tests. M. Cui, L. Liu, S.-Q. Ning, and S.-Y. Hao provided support for energetic performance tests. Y. Shang and X.-M. Chen provided guidance for data interpretation and manuscript preparation. All authors participated in the writing of the manuscript and provided comments.

Competing interests

Sun Yat-sen University has filed a Chinese patent application (No. 202511845814.X) related to this work.

Supplemental information

Tables of selected synthetic conditions for **CA**-based primary explosives with superior initiating efficiency to **LA**, crystallographic data and structure refinements for **ICA-1**, selected bond distances (Å) for **ICA-1**, selected unbonded N···N distances (Å) for **ICA-1**, the results of the long-term thermal stability test of **ICA-1**, independent elastic constants C_{ij} (GPa) of **LA**, **CA**, and **ICA-1**, polycrystalline VRH moduli and anisotropy indices of **LA**, **CA**, and **ICA-1**, cauchy pressures (GPa) of **LA**, **CA**, and **ICA-1**, input ignition energy evaluation tests for **LA**, input ignition energy evaluation tests for **ICA-1**; Figures of traditional lead-based primary explosives, such as $Pb(N_3)_2$ (**LA**) and lead styphnate (**LS**), new energetic compounds, different strategies for breaking through the bottleneck in the current compound system, this work proposes a strategy of cation-intercalalated copper azide layers by employing disc-shaped cations as intercalants to a deeply passivate **CA** derivative, optical images of **ICA-1**, the IR spectra of **ICA-1**, facile transformation of **CA** to **ICA-1** at room temperature *via* the Et_4N^+ cation intercalation and N_3^- ions supplementation, structure of the minimum asymmetric unit of **ICA-1**, the coordination modes of crystallographically independent Cu(II) atoms in **ICA-1**, the bridging modes of all N_3^- ions in **ICA-1**, coordination modes of Cu(II) ions and N_3^- anions in one single layer of **ICA-1** within the unit cell, structure of two distinct types of infinite 1D chains extending along the *a* axis, the shortest non-bonding N···N contact distance in pure **CA**,

the packing mode of Et_4N^+ cations, the non-covalent interactions of Et_4N^+ cations, DTA curve of **ICA-1** with a heating rate of 5 °C·min^{-1}, quartz tube shattered during DTA test, flame test of **ICA-1**, hot plate test of **ICA-1**, evaluation of the detonation output capability, detonation process for MPC determination captured by conventional camera, schematic of the experimental setup for input ignition energy evaluation, ignition events captured in input ignition energy evaluation tests (charging voltage: 3 V), snapshots of the detonation process of **ICA-1** as a primary charge in an energetic chip (PDF).

Supplementary Files

This is a list of supplementary files associated with this preprint. Click to download.

- cifandcheckcif.zip
- NatureSI.pdf
- SIvideo.zip